CrossMark

Influence of synthesis temperature on cobalt metal-organic framework (Co-MOF) formation and its electrochemical performance towards supercapacitor electrodes

Wenlu Xuan[1] · Rajendran Ramachandran[1,2,3] · Changhui Zhao[1,2] · Fei Wang[1,2,4]

Abstract

We have synthesized cobalt metal-organic framework (Co-MOF) at different temperatures through solvothermal route as metal-organic frameworks which can be used for supercapacitors. The effect of synthesizing temperature on Co-MOF's structure and porous behavior were analyzed with various characterization techniques like X-ray diffraction, Brunauer-Emmett-Teller surface analyzer, scanning electron microscope, and transmission electron microscope. The charge storage performance of the as-prepared Co-MOF's was carried out in 3 M KOH. The results proved the excellent redox behavior of Co-MOFs, and a maximum specific capacitance of 952.5 F g^{-1} was obtained for Co-MOF/150 (synthesized at 150 °C) at a current density of 0.25 A g^{-1}. The higher specific surface area and micropore of Co-MOF/150 significantly heightened the electrolyte ion transport during the electrochemical performance.

Introduction

Caused by fossil fuel-based energy sources, global warming, and environmental pollution problems have brought a few crucial issues, which drives many recent research attempts on exploring new materials for energy storage and energy conversion devices [1, 2]. The development of energy storage devices with high energy and power output, long lifetime, and short charging time is essential for many applications which include electric vehicles, energy storage for wind and large industrial equipment. Supercapacitors, also called electrochemical capacitors or ultracapacitors had attracted much attention in recent decades due to their characteristics of high-power density (> 10 kW kg^{-1}), long-term stabilities (> 10^5 cycles), high reliability, fast charge/discharge rate, and safe operation mode compared to traditional batteries [3, 4]. Depending on the charge storage processes, supercapacitors can be divided into the electrical double layer capacitors (EDLCs) and pseudocapacitors. EDLCs can store charges from electrostatic charge accumulation at electrode/electrolyte interface. The capacitive behavior of EDLCs mainly depends on the specific surface area and the structure of the electrode materials. Generally, carbon-based materials such as carbon nanotubes, activated carbon, graphene, and recently graphdiyne have been used for EDLCs due to their high surface area and excellent conductivity [5–9]. Pseudocapacitors can store charges due to the reversible faradic reactions involving charge transfer between electrode and electrolyte. Metal oxides, transition metal chalcogenides, and conducting polymers have been employed for pseudocapacitors thanks to their excellent redox activities and multiple available oxidation states [10–12]. In recent years, metal-organic frameworks (MOFs) have received much research interest in pseudocapacitors as a result of their high

✉ Fei Wang
wangf@sustc.edu.cn

1   Department of Electrical and Electronic Engineering, Southern University of Science and Technology (SUSTech), Shenzhen 518055, China

2   Shenzhen Key Laboratory of 3rd Generation Semiconductor Devices, Shenzhen 518055, China

3   SUSTech Academy for Advanced Interdisciplinary Studies, Shenzhen 518055, China

4   State Key Lab of Transducer Technology, Shanghai Institute of Microsystem and Information Technology, Chinese Academy of Sciences, Shanghai 200050, China

accessible surface area and porosity, tunable pore size, and ordered crystalline structures [13–18].

Metal-organic frameworks are a kind of porous materials connected with metal-containing units and organic linkers, and possess large surface area [13]. In recent years, several studies have been focused on MOF-based applications such as gas storage [19–22], separations [23–26], and catalysis [27–29]. Since metal cations (ions) inside the MOF can offer more active sites for redox behavior towards charge storage phenomena, many metals such as Cu [30, 31], Co [32–34], Ni [35–37], Fe [38], Cr [39], and Zr [40] have been used for MOFs as supercapacitor electrode materials. Among various MOFs, Co-MOF has received much attention in electrochemical energy storage devices such as lithium-ion batteries and supercapacitors due to its excellent redox performance. Cobalt, as a transition metal, can provide redox-active sites and is suitable to construct MOFs of good electrochemical performance. Furthermore, different oxidation states of cobalt could be involved in surface faradic redox reactions and delivered higher electrochemical activities than other MOF materials. Diaz et al. reported the electrochemical behavior of a Co-based MOF as electrode material firstly [33]. Lee et al. reported a Co-MOF synthesis and the electrode exhibited a specific capacitance of 179.2 F g^{-1}, an energy density of 31.4 Wh kg^{-1} and a power density of 5.64 kW kg^{-1} [41]. In some previous works, Co-MOFs showed good capacitive behavior with comparable specific capacitance and good cycling stability [34, 42]. It has been remarked that the electrochemical capacitance performance of the electrodes not only depends on the type of electrode, also it depends on the several factors such as morphology, porosity, size, and composition. The morphology, phase, and porous features of MOF can be controlled with synthesis conditions, including temperature, metal precursor, organic linker, molar concentration, and solvents.

In this paper, we have conducted a systematic study of temperature influence on Co-MOF synthesis using ethanol as solvent. The structure and porosity features of the as-prepared Co-MOF's were characterized, and their electrochemical performance was evaluated towards an electrode material of supercapacitors. The results suggested that the Co-MOF synthesized at 150 °C showed remarkable electrochemical performance with the specific capacitance of 956 F g^{-1} at a current density of 0.25 A g^{-1}, respectively. The large specific surface area and micropore structure of Co-MOF/150 lead to superior electrochemical performance towards supercapacitor applications.

Experimental methods

Materials

AR grade of cobalt (II) nitrate hexahydrate ($Co(NO_3)_2 \cdot 6H_2O$), 1,3,5-tricarboxylic acid (H_3BTC), was purchased from Sigma-Aldrich. Ethanol (99.8% assay) and potassium hydroxide (KOH) were purchased from Shanghai Lingfeng Chemical Reagent Co., LTD, China. The purchased chemicals were utilized without additional purification. Milli-Q water with pH 7.2 was used for all the solution preparation.

Preparation of Co-MOF

Different structures of Co-MOF's were synthesized at various temperatures by the following procedure. In the beginning,
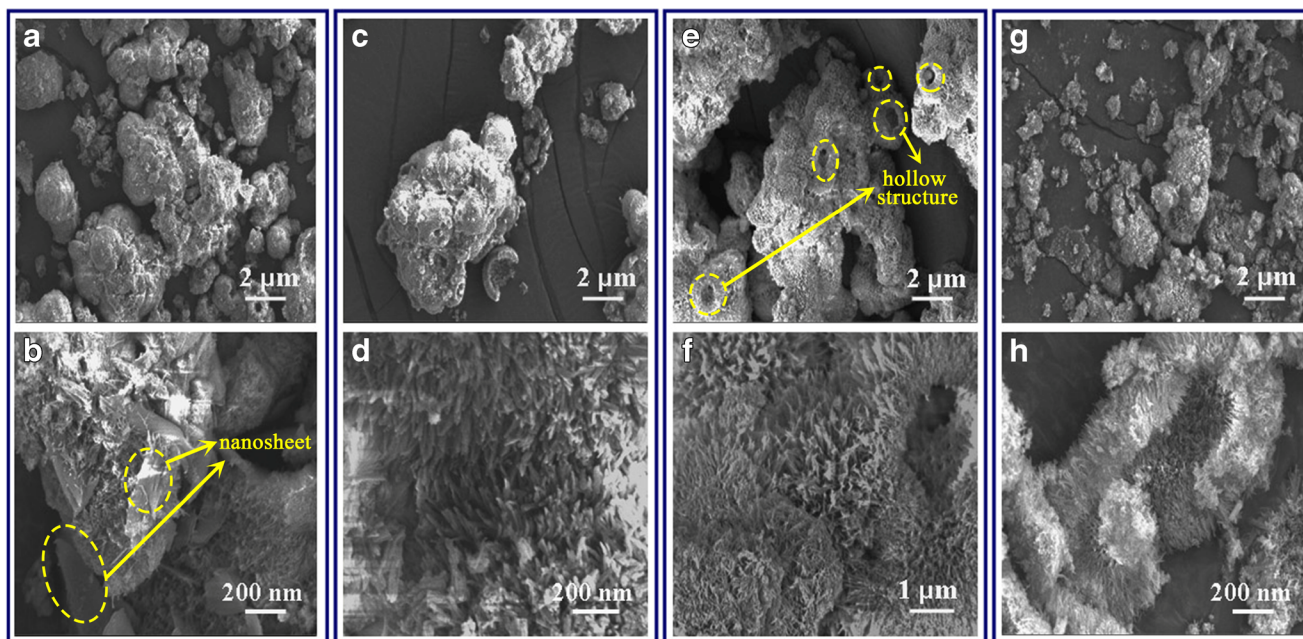
Fig. 1 SEM images of Co-MOF (**a**, **b**) Co-MOF/120 (**c**, **d**) Co-MOF/150 (**e**, **f**) Co-MOF/180, and (**g**, **h**) Co-MOF/210
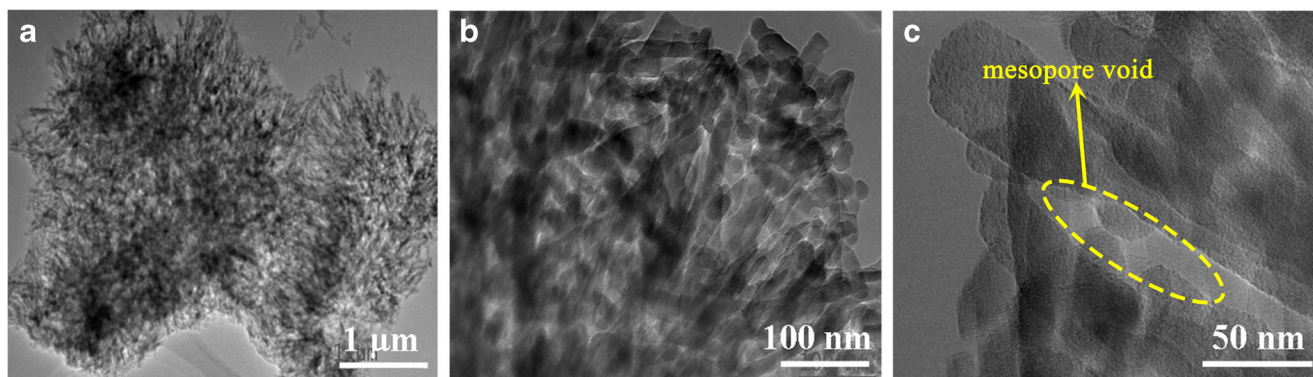
Fig. 2 TEM images of Co-MOF/150 at different magnifications

0.9 g of H_3BTC and 48 ml of ethanol solution were added together and agitated with a magnetic stirrer for 10 min. Following that, 1.8 g of $Co(NO_3)_2 \cdot 6H_2O$ was added to the previous solution and continued mixing for an additional 10 min. Later, the mixed solution was shifted into a Teflon-lined stainless steel autoclave (70 ml capacity) and heated at 120 °C for 12 h. After being cooled to room temperature naturally, the obtained purple color precipitate was thoroughly washed and centrifuged with ethanol several times. Finally, the collected sample was placed in a vacuum oven at 60 °C and dried for 24 h. As the prepared sample was marked as Co-MOF/120. The synthesis of Co-MOF/150, Co-MOF/180, and Co-MOF/210 was similar to that illustrated above with different temperatures at 150 °C, 180 °C, and 210 °C, respectively.

Material characterization

Powder X-ray diffraction pattern of Co-MOF samples was obtained by Rigaku Smartlab diffractometer with Cu-Kα radiation ($\lambda = 1.540$ Å). The surface morphologies and structures of the samples were observed using scanning electron microscope (Zeiss Merlin). In addition, the morphology of Co-MOF/150 was characterized with transmission electron microscope (FEI Tecnai F30). The textural porosity and specific surface area were analyzed with BET analyzer (Model: ASAP 2020).

Electrochemical measurements

Electrochemical workstation (CHI 660 E) was used for all the electrochemical measurements such as cyclic voltammetry (CV), galvanostatic charge-discharge (GCD) and electrochemical impedance spectroscopy (EIS) in 3 M KOH electrolyte. Active material (Co-MOF)-coated Ni foam was used as a working electrode with respect to a reference electrode of Ag/AgCl. Platinum (Pt) wire was employed as a counter electrode. The slurry-coated working electrode was fabricated as follows: In brief, active material and carbon black (conductive agent) with a mass ratio of 85:10 was mixed with 5 wt% of Nafion solution

to form a homogeneous slurry. Afterward, the slurry was coated on Ni foam electrode (2 cm × 1 cm × 0.1 cm). The total mass of the active material of electrode was 2 mg cm^{-2} and the total coated surface area was 1×1 cm^2. Finally, the electrode was allowed to dry at room temperature for 3 h. All the electrochemical studies were carried out under ambient conditions. The EIS spectrum of Co-MOF samples was fitted with ECLab software.

Results and discussion

The morphology of as-prepared Co-MOFs at different temperatures is shown in Fig. 1. From the SEM images, it could be seen that the hierarchical hollow microspheres of Co-MOFs are densely composed of one-dimensional nanorods, and the size of the obtained urchin-like Co-MOF spheres is
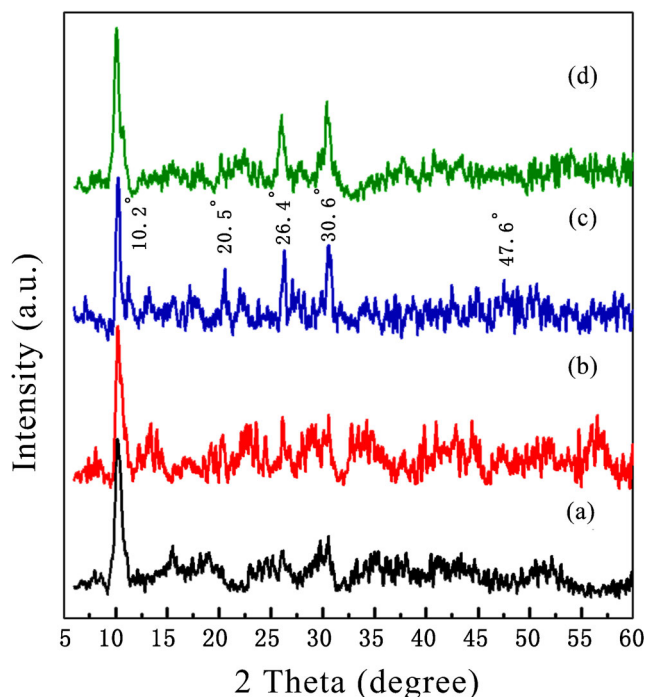
Fig. 3 XRD patterns of **a** Co-MOF/120, **b** Co-MOF/150, **c** Co-MOF/180, and **d** Co-MOF/210
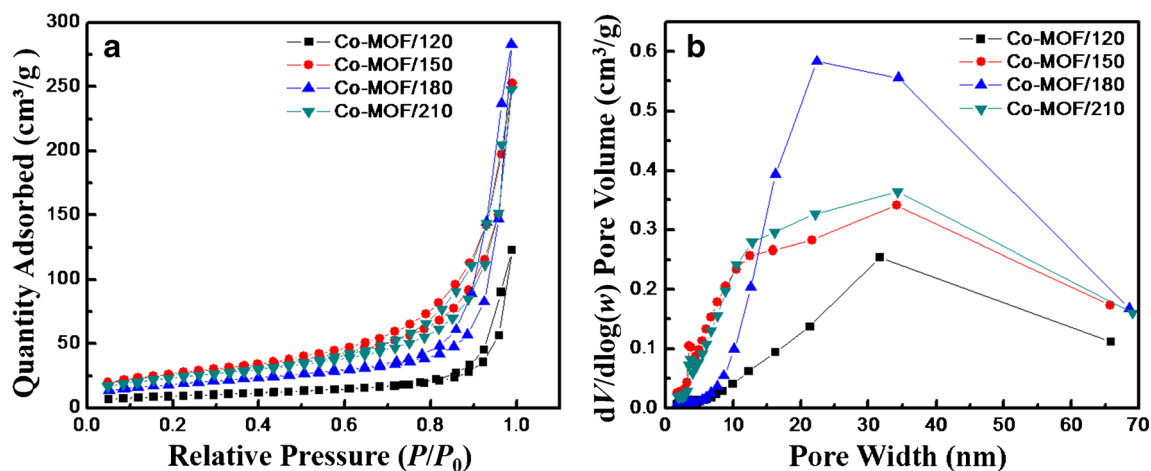
Fig. 4 **a** Nitrogen absorption-desorption isotherms of Co-MOF/120, Co-MOF/150, Co-MOF/180, and Co-MOF/210. **b** Pore size distribution calculated by BJH model

about 2 μm. It is unusual that some of nanosheets structure has been noticed in Co-MOF/120 sample, and the obtained nanosheets might be the reason to reduce the porous feature of MOF as discussed later in BET analysis. The sheet-like structure disappears in Co-MOF/150, indicating a different nucleation rate due to the higher temperature, which suggests that temperature could play an essential role in the formation of various MOF structures. The hollow structures of Co-MOF and the size of holes in the microspheres were expanded at the temperature 180 °C i.e., almost all the Co-MOF spheres became hollow structures compared with Co-MOF/120 and Co-MOF/150. At very high temperature (210 °C), most of the hollow microspheres disappear, and irregular shapes of MOF have been observed. As the evidence of the SEM analysis, the synthesis temperature plays a crucial role on the structure of Co-MOF concerning initial nucleation rates. TEM analysis further characterized the architectures of Co-MOF nanorod. Uniform sized nanorods was observed from TEM images of Co-MOF/150 sample (Fig. 2a–c), and the length and width of the nanorods are about 100 nm and 40 nm, respectively. It can be seen that the mesoporous of voids between the nanorods, and these voids can improve the electron transport and enhance the active sites for electrochemical reactions.

The crystallinity of the Co-MOF was investigated by X-ray diffraction (XRD), as shown in Fig. 3. The obtained

diffraction peaks agree well with the previously reported Co-MOF [43]. It is noticed that there was no apparent difference in the diffraction peaks among the Co-MOFs except the diffraction intensities. The difference in their intensities was mainly attributed to the presence of water or solvent molecules in MOF pores.

The textural characteristic such as porosity and specific surface area of as-prepared Co-MOFs were analyzed with BET analyzer. The N_2 adsorption-desorption isotherms of Co-MOF samples at 77 K in the relative pressure P/P_0 ranging from 0 to 1 are shown in Fig. 4a. The presence of the mesoporous structure in as-prepared Co-MOF samples was validated from type IV hysteresis isotherm loop at the relative pressure between 0.8 and 1.0 [44]. In addition, the mesoporous structure in the Co-MOF hollow spheres was further confirmed with BJH size distribution (Fig. 4b) and the curves show the centered peak in between 20 to 35 nm for all the synthesized Co-MOFs. Since the real pores were not discerned in the nanorods, we assume that the mesoporous behavior may come from the voids among the nanorods (indicated in Fig. 2c) [45]. The textural characteristics of the Co-MOFs are listed in the Table 1. The presence of nanosheets in Co-MOF/120 could reduce the voids between the nanorods, and lower its surface area and porous behavior. The large BET surface area (93.6 m^2 g^{-1}) and micropore area (2.60 m^2 g^{-1}) of Co-MOF/150 could promote the electrolyte ion migration

| Table 1 Textural characteristic observed from BET analysis of Co-MOF/120, Co-MOF/150, Co-MOF/180, and Co-MOF/210	Sample	BET surface area (m^2 g^{-1})	Micropore area (m^2 g^{-1})	External surface area (m^2 g^{-1})	Total pore volume (cm^3 g^{-1})	Micropore volume (cm^3 g^{-1})	Average pore size (nm)
	Co-MOF/120	31.9884	2.4268	29.5616	0.190407	0.001062	23.80948
	Co-MOF/150	93.6123	2.6072	91.0051	0.390774	0.000657	16.69754
	Co-MOF/180	65.2707	1.8006	63.4702	0.438348	0.000469	26.86336
	Co-MOF/210	83.4753	0.0733	83.4020	0.383602	0.000627	18.38155
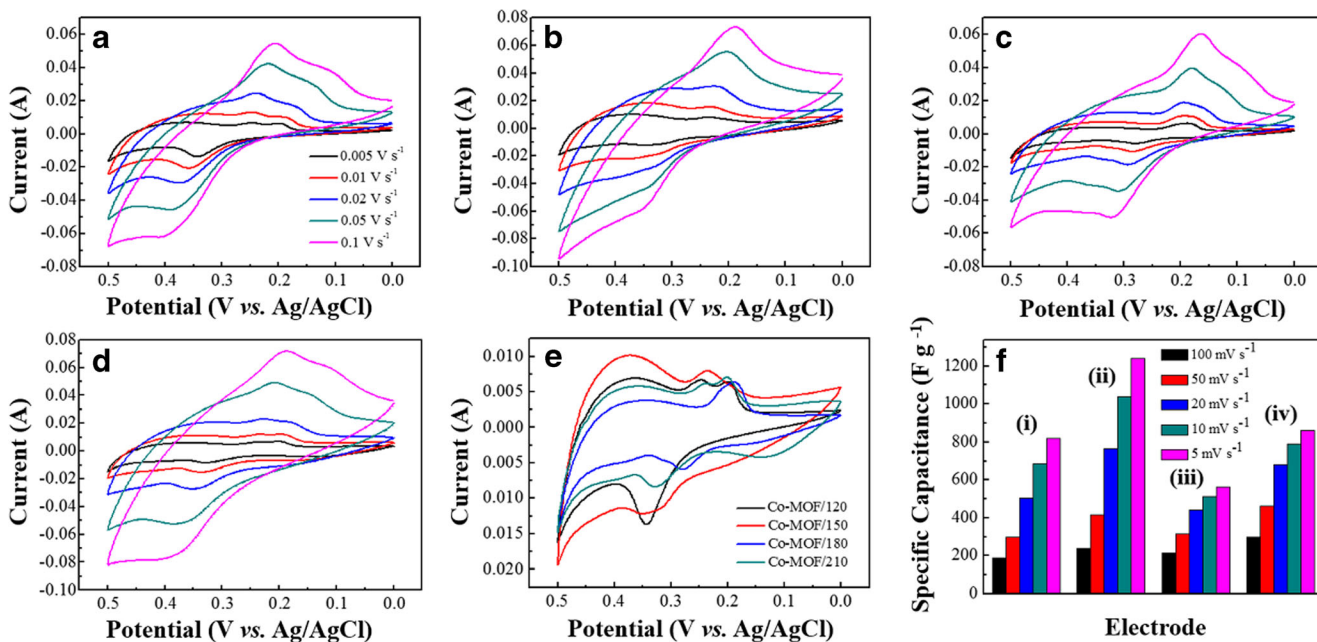
Fig. 5 Cyclic voltammogram (CV) curves of **a** Co-MOF/120, **b** Co-MOF/150, **c** Co-MOF/180, and **d** Co-MOF/210 at different scan rates. **e** Comparison of galvanostatic charge-discharge curve of Co-MOF/120, Co-MOF/150, Co-MOF/180, and Co-MOF/210 at 5 mV s^{-1} (**f**). Specific capacitance plot of Co-MOF electrodes at different scan rates (i) Co-MOF/120, (ii) Co-MOF/150, (iii) Co-MOF/180, and (iv) Co-MOF/210

between the electrode/electrolyte interface and boost the electrochemical redox reactions [46].

In order to evaluate the electrochemical supercapacitance performance of as-synthesized Co-MOFs electrodes, electrochemical measurements were investigated in 3 M KOH electrolyte from 0 to 0.5 *V* potential window. The cyclic

voltammetry performance of the Co-MOF electrodes is shown in Fig. 5. A couple of redox peaks is observed in the curves, suggesting the pseudocapacitance behavior of Co-MOF electrodes which comes from the faradic redox reactions of various cobalt oxidation states and the possible cobalt conversion involved in the electrochemical reactions can be described by
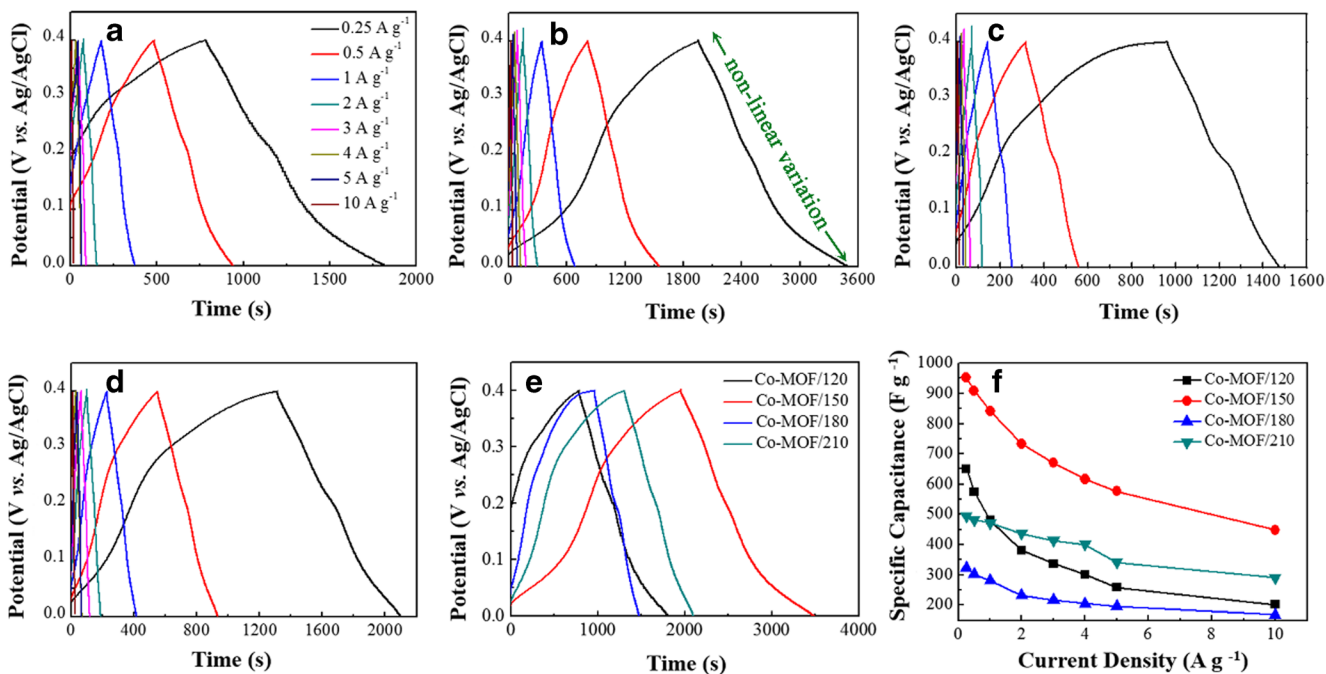
Fig. 6 Galvanostatic charge-discharge profile of **a** Co-MOF/120, **b** Co-MOF/150, **c** Co-MOF/180, and **d** Co-MOF/210 at different current densities. **e** Comparison of galvanostatic charge-discharge curve of Co-
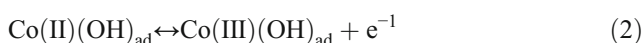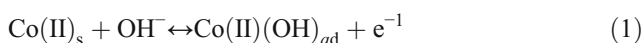
MOF electrodes at a current density of 0.25 A g^{-1} (**f**) specific capacitance plot of Co-MOF/120, Co-MOF/150, Co-MOF/180, and Co-MOF/210 at different current densities

Table 2 Comparison of specific capacitance of Co-MOF electrodes in this work with previously reported other Co-MOF electrodes

MOF	Synthesis condition	Solvent	C (F g^{-1})	Current density/scan rate	Electrolyte	Potential window (V)	Ref
Ni/Co-MOF nanoflakes	Ultrasonic irradiation and centrifugation	Methanol	530.4	0.5 A g^{-1}	1 M LiOH	0 to 0.5	18
ZIF-67	Ultrasonic irradiation	Methanol	168.3	0.5 A g^{-1}	1 M LiOH	0 to 0.5	18
Co-MOF-71	Hydrothermal—100 °C (50 h)	N,N-Dimethylformamide	206.76	0.6 A g^{-1}	1 M LiOH	0 to 0.5	32
Co-BDC	Hydrothermal—100 °C (50 h)	N,N-Dimethylformamide	131.8	10 mV s^{-1}	0.5 M LiOH	0 to 0.6	42
Co-NDC	Hydrothermal—180 °C (72 h)	Benzene/water	147.3	10 mV s^{-1}	0.5 M LiOH	0 to 0.6	42
Co-BPDC	Diffusion	Water	179.2	10 mV s^{-1}	0.5 M LiOH	0 to 0.6	42
Co-MOF/120	Hydrothermal—120 °C (12 h)	Ethanol	649.8	0.25 A g^{-1}	3 M KOH	0 to 0.4	This work
Co-MOF/150	*Hydrothermal—150 °C (12 h)*	*Ethanol*	*952.5*	*0.25 A g^{-1}*	*3 M KOH*	*0 to 0.4*	*This work*
Co-MOF/180	Hydrothermal—180 °C (12 h)	Ethanol	322.1	0.25 A g^{-1}	3 M KOH	0 to 0.4	This work
Co-MOF/210	Hydrothermal—210 °C (12 h)	Ethanol	495.6	0.25 A g^{-1}	3 M KOH	0 to 0.4	This work

This condition provides the best capacitance value comparing with the other results listed in the table

the following expression [47].

$$Co(II)_s + OH^- \leftrightarrow Co(II)(OH)_{ad} + e^{-1} \qquad (1)$$

$$Co(II)(OH)_{ad} \leftrightarrow Co(III)(OH)_{ad} + e^{-1} \qquad (2)$$

The area of CV curve represents the capacitance behavior of the electrodes. As shown in the Fig. 5e, both the measured current level and the area of the curve from Co-MOF/150 electrode were higher than those of all the other electrodes which indicates the best capacitive behavior. The specific capacitance of the electrodes from CV curves was calculated according to the following formula [48],

$$C = \frac{1}{m \times v \times (Vc - Va)} \times \int_{Va}^{Vc} I(V) dV \qquad (3)$$

where v is the scan rate; m is the mass of the active material of the electrode; V_a is the anodic potential; V_c is the cathodic potential; $I(V)$ is the response current density versus potential and V is the potential. As compared in Fig. 5f, a maximum specific capacitance of 1240.4 F g^{-1} has been attained for the Co-MOF/150 electrode at a scan rate of 5 mV s^{-1} which is higher compared to other electrodes due to the better ion transport within the mesoporous voids structures [49]. The specific capacitance of electrode decreases with the increase of scan rate, which is due to the insufficient redox reactions at high scan rates.

In addition, the specific capacitance behavior of the electrodes was characterized by galvanostatic charge-discharge (GCD) technique, and the GCD curves of the electrodes are shown in Fig. 6. The non-linear changes in charge and discharge curves (indicated in Fig. 6b) are attributed to the good pseudocapacitance behavior of the electrodes which is consistent with the CV results [50]. The following expression is used for electrodes specific capacitance calculation from GCD

measurement [51, 52],

$$C = \frac{I \times \Delta t}{m \times \Delta V} \qquad (4)$$

where Δt is the discharge time (s), I is the applied current (A), m is the total mass of the active material of the electrode (g), ΔV is the potential window (V). A maximum specific capacitance of 952.5 F g^{-1} has been achieved for the Co-MOF/150 electrode at a current density of 0.25 A g^{-1}. With the same current density, however, the other electrodes exhibit a lower specific capacitance of 649.8, 322.1 and 495.6 F g^{-1} for Co-MOF/120, Co-MOF/180, Co-MOF/210, respectively (Fig. 6f). The larger specific surface area and higher micro-pore area of Co-MOF/150 enhance the electrolyte ion transportation to the electrode and deliver better redox behavior. Table 2 shows a comparison of the current work with previously reported electrodes based on MOF materials. The cyclic stability of the
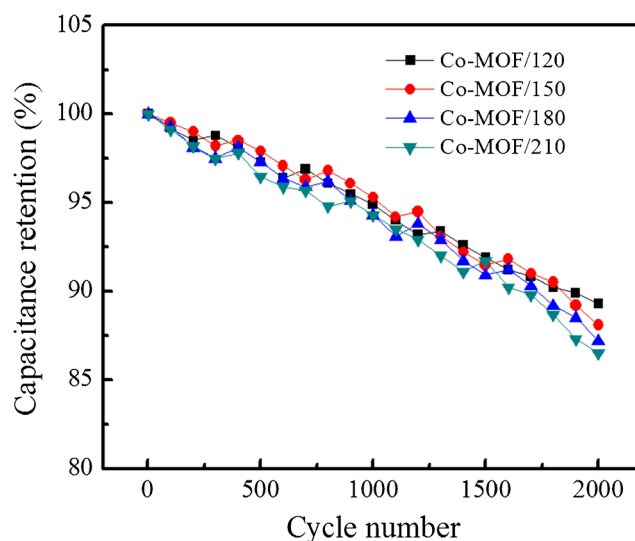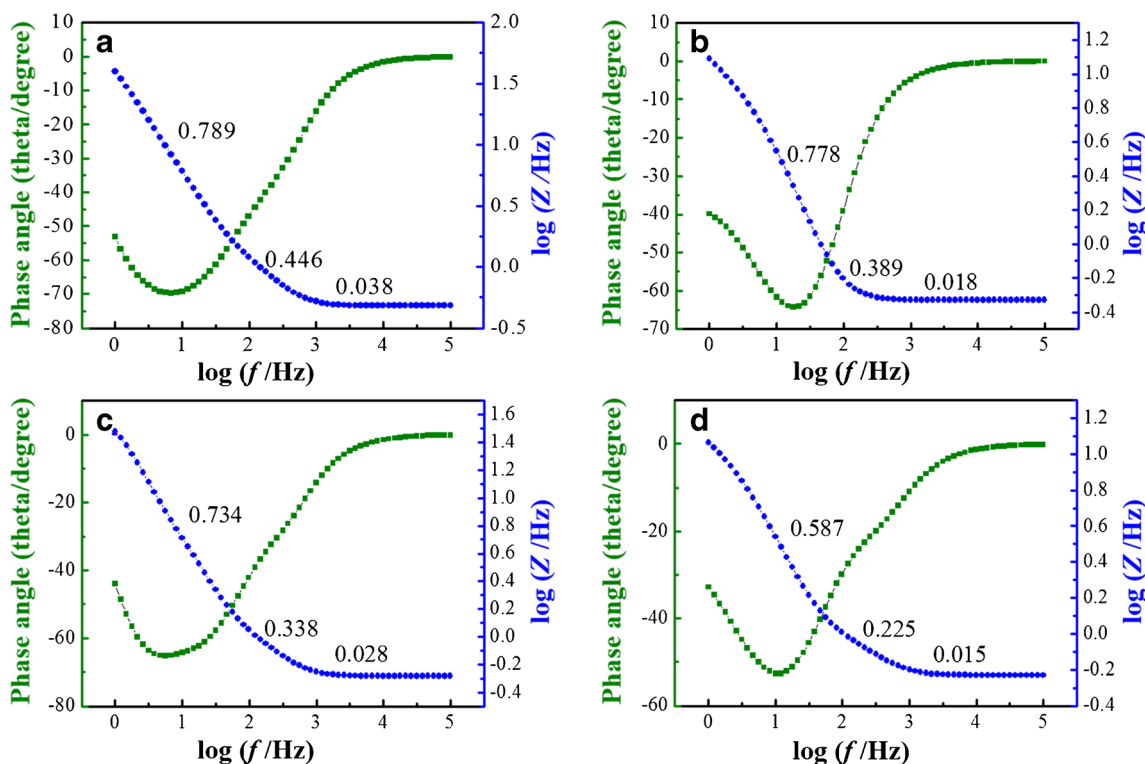

Fig. 7 Specific capacitance retention behavior of Co-MOF electrodes at 5 A g^{-1} current density
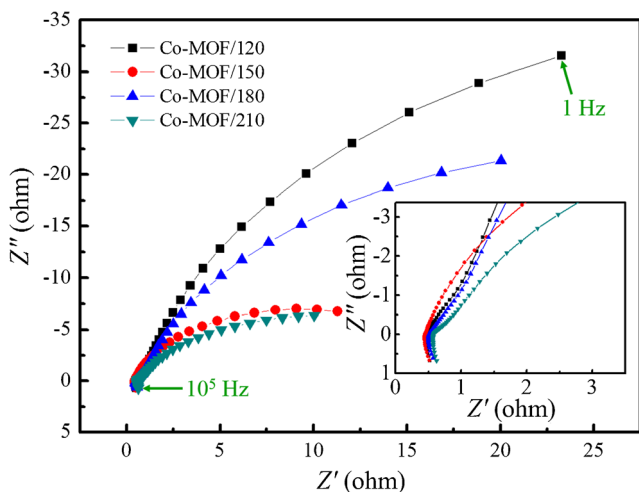
Fig. 8 Nyquist plot of Co-MOF electrodes from the frequency range of 1 Hz to 105 Hz

Electrochemical impedance analysis was investigated to understand the ion transfer phenomenon of the electrode/electrolyte interface. Nyquist plot of the Co-MOF electrodes is shown in Fig. 8. The intercept at the real axis in the high-frequency region corresponds to the solution resistance (R_s) of the electrode/electrolyte interface. [53]. It could be seen that the R_s value of Co-MOF/150 electrode shows a minor value (inset picture of Fig. 8) than others which suggesting better conductivity and better electrolyte ion transportation in the electrode/electrolyte interfaces [54]. The Nyquist plot of Co-MOF/150 electrode before and after 2000 cycles is shown in Fig. S2. As the evidence from the figure, the solution resistance at the high-frequency region is increased after cycles, suggesting that the decreased ion mobilities during the long cyclic process. However, the straight line at lower frequency region is closer to the imaginary axis which indicates that better pseudocapacitive nature and good stability even after cycles. The bode phase angle of Co-MOF the electrodes (Fig. 9) is obtained in the range of 50°–70° at low-frequency region (< 100 Hz) which is attributed to the perfect pseudocapacitance function of electrodes [55]. The higher phase angle of Co-MOF/150 demonstrates better transportation of electrolyte ions and hence achieved greater pseudocapacitance response. The plot of total impedance versus frequency shows three different slopes at different frequency regions. The slope at higher frequency region (10^5–10^3 Hz) of all the Co-MOF electrodes exhibited almost zero suggesting that the electrode and electrolyte ions interactions

electrodes was investigated by GCD endurance test at 5 A g^{-1} current density for 2000 cycles (Fig. 7). It can be seen that the specific capacitance retains to be over 85% after 2000 cycles for all the Co-MOF electrodes which suggesting the good electrochemical reversibility during charge/discharge process. The changes in the morphology of Co-MOF/150 electrode was analyzed before and after 2000 cycles and shown in Fig. S1. As the evidence of the figure, the tiny change in the morphology is remarked which suggests that the Co-MOF microspheres undergo considerable aggregation during the long cyclic process.

Fig. 9 Bode plots of **a** Co-MOF/120, **b** Co-MOF/150, **c** Co-MOF/180, and **d** Co-MOF/210 electrodes

became weaker, and a resistive component is dominant. Whereas, at the low-frequency (< 100 Hz) and the mid-frequency regions (10^3–10^2 Hz), the value of the slopes are higher and these can be associated to the greater adsorption of the electrolyte ions onto the electrode surface, thus confirmed the pseudocapacitive nature of Co-MOF electrodes.

Overall, the higher specific capacitance of the Co-MOF/150 electrode can be attributed to the subsequent reasons: (1) the large surface area of the Co-MOF/150 from hollow microspheres guarantees excellent redox-active sites for charge storage, which ends up in high electrochemical performance; (2) a larger micropore area and also the mesoporous voids could reduce the ion diffusion path to the electrode, which often makes sure good rate capability.

Conclusion

In summary, we have synthesized Co-MOF at different temperatures and characterized their performance with various tools. Based on the structure and porous analysis, we have optimized the temperature for obtaining large surface area of Co-MOF. The electrochemical properties of as-prepared Co-MOFs were examined towards electrode material of supercapacitor in 3 M KOH electrolyte. A maximum specific capacitance of 952.5 F g^{-1} has been obtained for Co-MOF/150 at a current density of 0.25 A g^{-1}. This excellent electrochemical characteristics of Co-MOF/150 may lead to a promising electrode for high-performance supercapacitors.

References

1. Krishnamoorthy K, Pazhamalai P, Kim SJ (2017) Ruthenium sulfide nanoparticles as a new pseudocapacitive material for supercapacitor. Electrochim Acta 227:85–94
2. Saranya M, Ramachandran R, Wang F (2016) Graphene-zinc oxide (G-ZnO) nanocomposite for electrochemical supercapacitor applications. J Sci Adv Mater Devices 1(4):454–460
3. Pu J, Wang X, Xu R, Komvopoulos K (2016) Highly stretchable microsupercapacitor arrays with honeycomb structures for integrated wearable electronic systems. ACS Nano 10(10):9306–9315
4. Sahoo S, Pazhamalai P, Krishnamoorthy K, Kim SJ (2018) Hydrothermally prepared α-MnSe nanoparticles as a new pseudocapacitive electrode material for supercapacitor. Electrochim Acta 268:403–410
5. Zhu Y, Murali S, Stoller MD, Ganesh KJ, Cai W, Ferreira PJ, Pirkle A, Wallace RM, Cychosz KA, Thommes M (2011) Carbon-based supercapacitors produced by activation of graphene. Science 332(6037):1537–1541
6. Zhang LL, Zhao X (2009) Carbon-based materials as supercapacitor electrodes. Chem Soc Rev 38(9):2520–2531
7. Wang X, Liu L, Wang X, Bai L, Wu H, Zhang X, Yi L, Chen Q (2011) Preparation and performances of carbon aerogel microspheres for the application of supercapacitor. J Solid State Electrochem 15(4):643–648
8. Pu J, Wang X, Zhang T, Li S, Liu J, Komnopoulos K (2016) High-energy-density, all-solid-state microsupercapacitors with three-dimensional interdigital electrodes of carbon/polymer electrolyte composite. Nanotechnol 27(4):045701
9. Krishnamoorthy K, Thangavel S, Veetil JC, Raju N, Venugopal G, Kim SJ (2016) Graphdiyne nanostructures as a new electrode material for electrochemical supercapacitors. Int J Hydrog Energy 41(3):1672–1678
10. Lang JW, Kong LB, Wu WJ, Luo YC, Kang L (2008) Facile approach to prepare loose-packed NiO nano-flakes materials for supercapacitors. Chem Commun 0(35):4213–4215
11. Abouali S, Garakani MA, Zhang B, Xu ZL, Heidari EK, Huang JQ, Huang J, Kim JK (2015) Electrospun carbon nanofibers with in situ encapsulated Co_3O_4 nanoparticles as electrodes for high-performance supercapacitors. ACS Appl Mater Interfaces 7(24):13503–13511
12. Pazhamalai P, Krishnamoorthy K, Mariappan VK, Sahoo S, Manoharan S, Kim SJ (2018) A high efficacy self-charging $MoSe_2$ solid-state supercapacitor using electrospun nanofibrous piezoelectric separator with ionogel electrolyte. Adv Mater Interfaces 5(12):1800055
13. Furukawa H, Cordova KE, O'Keeffe M, Yaghi OM (2013) The chemistry and applications of metal-organic frameworks. Science 341(6149):1230444
14. Xia W, Mahmood A, Zou R, Xu Q (2015) Metal-organic frameworks and their derived nanostructures for electrochemical energy storage and conversion. Energy Environ Sci 8(7):1837–1866
15. Salunkhe RR, Kaneti YV, Kim J, Kim JH, Yamauchi Y (2016) Nanoarchitectures for metal–organic framework-derived nanoporous carbons toward supercapacitor applications. Acc Chem Res 49(12):2796–2806
16. Gao W, Chen D, Quan H, Zou R, Wang W, Luo X, Guo L (2017) Fabrication of hierarchical porous metal-organic framework electrode for aqueous asymmetric supercapacitor. ACS Sustain Chem Eng 5(5):4144–4153
17. Shi C, Wang X, Gao Y, Rong H, Song Y, Liu H-J, Liu (2017) Nickel metal-organic framework nanoparticles as electrode materials for Li-ion batteries and supercapacitors. J Solid State Electrochem 21(8):2415–2423
18. Ramachandran R, Zhao C, Luo D, Wang K, Wang F (2017) Synthesis of copper benzene-1, 3, 5-tricarboxylate metal organic frameworks with mixed phases as the electrode material for supercapacitor applications. Appl Surf Sci. https://doi.org/10.1016/j.apsusc.2017.11.271
19. Tsivion E, Mason JA, Gonzalez MI, Long JR, Head-Gordon M (2016) A computational study of CH_4 storage in porous framework materials with metalated linkers: connecting the atomistic character of CH_4 binding sites to usable capacity. Chem Sci 7(7):4503–4518
20. Rosi NL, Eckert J, Eddaoudi M, Vodak DT, Kim J, O'keeffe M, Yaghi OM (2003) Hydrogen storage in microporous metal-organic frameworks. Science 300(5622):1127–1129
21. Gao CY, Tian HR, Ai J, Li LJ, Dang S, Lan YQ, Sun ZM (2016) A microporous Cu-MOF with optimized open metal sites and pore spaces for high gas storage and active chemical fixation of CO_2. Chem Commun 52(74):11147–11150
22. Alezi D, Belmabkhout Y, Suyetin M, Bhatt PM, Weseliński ŁJ, Solovyeva V, Adil K, Spanopoulos I, Trikalitis PN, Emwas AH, Eddaoudi M (2015) MOF crystal chemistry paving the way to gas

storage needs: aluminum-based soc-MOF for CH_4, O_2, and CO_2 storage. J Am Chem Soc 137(41):13308–13318

23. Bárcia PS, Zapata F, Silva JA, Rodrigues AE, Chen B (2007) Kinetic separation of hexane isomers by fixed-bed adsorption with a microporous metal−organic framework. J Phys Chem B 111(22):6101–6103

24. Li K, Olson DH, Lee JY, Bi W, Wu K, Yuen T, Xu Q, Li J (2008) Multifunctional microporous MOFs exhibiting gas/hydrocarbon adsorption selectivity, separation capability and three-dimensional magnetic ordering. Adv Funct Mater 18(15):2205–2214

25. Hu J, Cai H, Ren H, Wei Y, Xu Z, Liu H, Hu Y (2010) Mixed-matrix membrane hollow fibers of $Cu_3(BTC)_2$ MOF and polyimide for gas separation and adsorption. Ind Eng Chem Res 49(24):12605–12612

26. Luo F, Yan C, Dang L, Krishna R, Zhou W, Wu H, Dong X, Han Y, Hu TL, O'Keeffe M, Wang L, Luo M, Lin RB, Chen B (2016) UTSA-74: a MOF-74 isomer with two accessible binding sites per metal center for highly selective gas separation. J Am Chem Soc 138(17):5678–5684

27. Wang C, DeKrafft KE, Lin W (2012) Pt nanoparticles@ photoactive metal-organic frameworks: efficient hydrogen evolution via synergistic photoexcitation and electron injection. J Am Chem Soc 134(17):7211–7214

28. Valvekens P, Vandichel M, Waroquier M, Speybroeck VV, Vos DD (2014) Metal dioxidoterephthalate MOFs of the MOF 74 type: microporous basic catalysts with well defined active sites. J Catal 317:1–10

29. Wu CD, Hu A, Zhang L, Lin W (2005) A homochiral porous metal– organic framework for highly enantioselective heterogeneous asymmetric catalysis. J Am Chem Soc 127(25):8940–8941

30. Srimuk P, Luanwuthi S, Krittayavathananon A, Sawangphruk M (2015) Solid type supercapacitor of reduced graphene oxide-metal organic framework composite coated on carbon fiber paper. Electrochim Acta 157:69–77

31. Harvey SD, Eckberg AD, Thallapally PK (2011) Evaluation of copper-1,3,5-benzenetricarboxylate metal–organic framework (Cu MOF) as a selective sorbent for Lewis base analytes. J Sep Sci 34(18):2418–2426

32. Lee DY, Yoon SJ, Shrestha NK, Lee SH, Ahn H, Han SH (2012) Unusual energy storage and charge retention in Co-based metal-organic frameworks. Microporous Mesoporous Mater 153:163–165

33. Díaz R, Orcajo MG, Botas JA, Calleja G, Palma J (2012) Co-MOF-5 as electrode for supercapacitors. Mater Lett 68:126–128

34. Yang J, Ma Z, Gao W, Wei M (2017) Layered structural Co-based MOF with conductive network frames as a new supercapacitor electrode. Chem Eur J 23(3):631–636

35. Wen P, Gong P, Sun J, Wang J, Yang S (2015) Design and synthesis of Ni-MOF/CNT composites and rGO/carbon nitride composites for an asymmetric supercapacitor with high energy and power density. J Mater Chem A 3(26):13874–13883

36. Yang J, Zheng C, Xiong P, Li Y, Wei M (2014) Zn-doped Ni-MOF material with a high supercapacitive performance. J Mater Chem A 2(44):19005–19010

37. Sheberla D, Bachman JC, Elias JS, Sun CJ, Shao-Horn Y, Dincă M (2016) Conductive MOF electrodes for stable supercapacitors with high areal capacitance. Nat Mater 16:220–224

38. Campagnol N, Romero-Vara R, Deleu W, Stappers L, Binnemans K, De Vos DE, Fransaer J (2014) A hybrid supercapacitor based on porous carbon and the metal-organic framework MIL-100 (Fe). ChemElectroChem 1(7):1182–1188

39. Jhung SH, Lee JH, Yoon JW, Serre C, Férey G, Chang JS (2007) Microwave synthesis of chromium terephthalate MIL-101 and its benzene sorption ability. Adv Mater 19(1):121–124

40. Choi KM, Jeong HM, Park JH, Zhang YB, Kang JK, Yaghi OM (2014) Supercapacitors of nanocrystalline metal–organic frameworks. ACS Nano 8(7):7451–7457

41. Lee DY, Shinde DV, Kim EK, Lee W, Oh IW, Shrestha NK, Lee JK, Han SH (2013) Supercapacitive property of metal–organic-frameworks with different pore dimensions and morphology. Microporous Mesoporous Mater 171:53–57

42. Wang L, Feng X, Ren L, Piao Q, Zhong J, Wang Y, Li H, Chen Y, Wang B (2015) Flexible solid-state supercapacitor based on a metal–organic framework interwoven by electrochemically-deposited PANI. J Am Chem Soc 137(15):4920–4923

43. Yu G, Sun J, Muhammad F, Wang P, Zhu G (2014) Cobalt-based metal organic framework as precursor to achieve superior catalytic activity for aerobic epoxidation of styrene. RSC Adv 4(73):38804–38811

44. Zhou G, Zhu J, Chen Y, Mei L, Duan X, Zhang G, Chen L, Wang T, Lu B (2014) Simple method for the preparation of highly porous $ZnCo_2O_4$ nanotubes with enhanced electrochemical property for supercapacitor. Electrochim Acta 123:450–455

45. An C, Wang Y, Huang Y, Xu Y, Jiao L, Yuan H (2014) Porous $NiCo_2O_4$ nanostructures for high performance supercapacitors via a microemulsion technique. Nano Energy 10:125–134

46. Jiao Y, Pei J, Yan C, Chen D, Hu Y, Chen G (2016) Layered nickel metal-organic framework for high performance alkaline battery-supercapacitor hybrid devices. J Mater Chem A 4(34):13344–13351

47. Liu X, Shi C, Zhai C, Cheng M, Liu Q, Wang G (2016) Cobalt-based layered metal–organic framework as an ultrahigh capacity supercapacitor electrode material. ACS Appl Mater Interfaces 8(7):4585–4591

48. Srinivasan V, Weidner JW (2002) Capacitance studies of cobalt oxide films formed via electrochemical precipitation. J Power Sources 108(1-2):15–20

49. Ramachandran R, Zhao C, Luo D, Wang K, Wang F (2018) Morphology-dependent electrochemical properties of cobalt-based metal organic frameworks for supercapacitor electrode materials. Electrochim Acta 267:170–180

50. Zhao YQ, Zhao DD, Tang PY, Wang YM, Xu CL, Li HL (2012) MnO_2/graphene/nickel foam composite as high performance supercapacitor electrode via a facile electrochemical deposition strategy. Mater Lett 76:127–130

51. Gao Y, Chen S, Cao D, Wang G, Yin J (2010) Electrochemical capacitance of Co_3O_4 nanowire arrays supported on nickel foam. J Power Sources 195(6):1757–1760

52. Liu XM, Zhang XG, Fu SY (2006) Preparation of urchinlike NiO nanostructures and their electrochemical capacitive behaviors. Mater Res Bull 41(3):620–627

53. Ramachandran R, Saranya M, Kollu P, Raghupathy BP, Jeong SK, Grace AN (2015) Solvothermal synthesis of zinc sulfide decorated graphene (ZnS/G) nanocomposites for novel supercapacitor electrodes. Electrochim Acta 178:647–657

54. Morozan A, Jaouen F (2012) Metal organic frameworks for electrochemical applications. Energy Environ Sci 5(11):9269–9290

55. Arul NS, Mangalaraj D, Ramachandran R, Grace AN, Han JI (2015) Fabrication of CeO_2/Fe_2O_3 composite nanospindles for enhanced visible light driven photocatalysts and supercapacitor electrodes. J Mater Chem A 3(29):15248–15258